Progress in Natural Science: Materials International 34 (2024) 676–681

HOSTED BY

Contents lists available at ScienceDirect

Progress in Natural Science: Materials International

journal homepage: www.elsevier.com/locate/pnsmi

Promoted reverse water-gas shift activity on transition metals-incorporated iron-cerium oxide solid solution catalyst

Yi Xie [1], Wenhao Qin [1], Linyu Wang, Yueren Liu, Haoyang Jiang, Miao Zhong [*]

College of Engineering and Applied Sciences, National Laboratory of Solid State Microstructures, The Frontiers Science Center for Critical Earth Material Cycling, Nanjing University, Nanjing, 210023, China

ARTICLE INFO

Keywords:
Reverse water-gas shift reaction
Solid solution
Ceria
Iron-based catalyst
Transition metal doping

ABSTRACT

Earth-abundant Fe oxide-based catalysts, renowned for their broad-spectrum light absorption, hold promise for driving the photothermal RWGS reaction—a promising strategy for converting CO_2 emissions into valuable carbonaceous feedstocks. However, traditional Fe oxide-based catalysts exhibit limited activity due to their constrained H_2 dissociation and CO_2 activation capabilities, especially at lower temperatures. This study introduces Co, Ni, and Cu-doped $Ce_{0.7}Fe_{0.3}O_2$ solid-solution catalysts. Incorporation of Fe into CeO_2 enhances CO_2 dissociation while preserving extensive light adsorption up to 2500 nm. Notably, Co doping enhances H_2 dissociation and promotes CO_2 activation. Subsequent investigations reveal that a catalyst doped with 5 mol% Co exhibits the highest photothermal catalytic activity, attaining a ~50 % CO_2 conversion under 300 W Xe-lamp irradiation with excellent selectivity and stability over 10 reaction cycles spanning 10 h. These results underscore the potential of designing CeO_2-based solid solution catalysts with synergistic metal dopants for efficient and selective CO_2 conversion under moderate conditions.

1. Introduction

Over the past few decades, efforts have been devoted to converting and utilizing carbon dioxide (CO_2) [1,2]. Among them, converting CO_2 into valuable fuels or chemical feedstocks through photothermal processes represents a cutting-edge CO_2 reduction technology [3,4]. The reverse water-gas shift (RWGS, $CO_2 + H_2 \rightarrow CO + H_2O$) reaction offers a strategic pathway to produce CO, a crucial platform molecule for various industrial processes such as Fischer-Tropsch and methanol synthesis [5]. This approach holds commercial potential due to its compatibility with existing industrial infrastructure. However, the RWGS reaction usually requires high temperatures to attain sufficient conversion. Additionally, the bond energy of C═O in CO_2, estimated at 803 kJ mol^{-1}, necessitates substantial energy input for activation [6–8]. The propensity for the side reaction—CO_2 methanation—further complicates the process by reducing the yield of the desired CO product [9]. To overcome these challenges, considerable efforts should be made to develop efficient photothermal catalysts for the RWGS reaction with high activities, selectivities, and long-term stabilities.

While noble metal catalysts such as Pt have shown excellent performance, their scarcity and high-cost limit the prospects for large-scale utilization. Therefore, there is a growing interest in developing non-noble transition metal catalysts that can enhance CO_2 to CO reaction rates at lower temperatures. Research has identified Fe, Co, Ni, and Cu as active metals in the RWGS reaction [10–13]. Among them, Ni and Co catalysts have shown superior CO_2 activation and conversion capabilities; however, they tend to over-reduce CO to CH_4 [10,13]. Cu catalysts, on the other hand, suffer from stability issues due to sintering at elevated temperatures [14]. Iron (Fe) stands out as an attractive candidate for catalyst development due to its natural abundance and the weak adsorption of *CO on Fe oxide surfaces, which results in high CO selectivity in the RWGS reaction via the CO_2 dissociative activation pathway [12]. Furthermore, Fe oxides-based catalysts exhibit remarkable resistance to sintering, even under extreme conditions such as continuous operation at temperatures above 600 °C [15]. Another significant advantage of Fe oxides-based catalysts is their strong light absorption and photothermal conversion capabilities, particularly in the visible and near-infrared spectrum [16]. This allows for the utilization of Fe oxides-based catalysts in solar-driven RWGS processes.

Despite the promising characteristics of Fe oxides-based catalysts, their inherent limitations in H_2 dissociation pose a significant challenge in enhancing catalytic activity for the RWGS reaction [17]. Recently, the

* Corresponding author.
E-mail address: miaozhong@nju.edu.cn (M. Zhong).
[1] These authors contributed equally: Yi Xie, Wenhao Qin.

https://doi.org/10.1016/j.pnsc.2024.05.011
Received 9 April 2024; Received in revised form 4 May 2024; Accepted 21 May 2024
Available online 22 July 2024

development of transition metal solid-solution catalysts, particularly those utilizing CeO_2 as the structural framework, has emerged as a breakthrough approach [3,18,19]. The efficiency of CO_2 dissociation on CeO_2-based catalysts is reliant on the availability of oxygen vacancies (V_O) on the surfaces. These catalysts have demonstrated remarkable performance in various CO_2 transforming reactions involving the production of CO, CH_4, and other hydrocarbon molecules [3,20,21]. Therefore, the integration of Fe sites into the CeO_2 lattice to form a solid-solution structure is considered a feasible strategy for achieving high RWGS activities. This solid solution configuration not only ensures the dispersion of active sites but also capitalizes on the rich surface oxygen vacancies in the CeO_2 structure. The synergistic effect between the Fe sites and the V_O in CeO_2 would be particularly beneficial in promoting efficient CO_2 adsorption and activation, which are essential for the RWGS reaction. Furthermore, the introduction of a third transition metal, such as Co, Ni, or Cu, presents an opportunity to improve the catalytic performance. The addition of these dopants can potentially enhance the H_2 dissociation, improving the RWGS kinetics beyond single-component Fe oxide catalysts [22,23].

In this study, we synthesized iron-cerium oxide ($Ce_{0.7}Fe_{0.3}O_2$) solid-solution catalysts doped with Co, Ni, and Cu, respectively. By employing low-concentration doping, we aimed to preserve the morphology and lattice structure of the $Ce_{0.7}Fe_{0.3}O_2$ solid solution. Our findings reveal that doping Co, Ni, and Cu in the 0.25–5 mol% range lowered the onset temperature for the RWGS reaction compared to the undoped $Ce_{0.7}Fe_{0.3}O_2$. In flow reaction experiments, the doped catalysts exhibited enhanced CO_2 conversions below 500 °C, coupled with high CO selectivity, and the most pronounced improvements were observed in the Co-doped samples. Characterization using temperature-programmed surface reaction (TPSR) and X-ray photoelectron spectroscopy (XPS) analyses before and after reactions indicated a reduced temperature for O^{2-} reduction on the catalyst surface and a slightly increased Fe^{2+}/Fe^{3+} ratio. These results suggest that Co doping enhances H_2 dissociation, thereby promoting the formation of highly active Fe^{2+}–V_O sites for CO_2 dissociative activation. We further investigated the impact of Co doping levels on catalytic performance and conducted photothermal batch reaction tests. The catalyst with 5 mol% Co doping demonstrated the highest activity, achieving a ~50 % CO_2 conversion under 1 h of Xe-lamp irradiation, with a unity CO selectivity, and maintained its activity over 10 reaction cycles of 10 h without deactivation as confirmed by morphological and structural characterizations of the catalyst before and after tests.

2. Materials and methods

2.1. Synthesis of catalysts

The synthesis of $M_{x\%}$:$Ce_{0.7}Fe_{0.3}O_2$, where M represents Co, Ni, or Cu and *x* represents the values 0, 0.25, 5, or 10, is carried out through a series of steps including co-precipitation, hydrothermal treatment, and annealing. First, 2.8 mmol of cerium (III) nitrate hexahydrate ($Ce(NO_3)_3{\cdot}6H_2O$) and 1.2 mmol of iron (III) nitrate nonahydrate ($Fe(NO_3)_3{\cdot}9H_2O$), along with varying amounts of the selected metal nitrate (cobalt (II) nitrate hexahydrate $Co(NO_3)_2{\cdot}6H_2O$ (0.01, 0.2, 0.4 mmol), nickel (II) nitrate hexahydrate ($Ni(NO_3)_2{\cdot}6H_2O$) (0.01 mmol), or copper (II) nitrate tetrahydrate ($Cu(NO_3)_2{\cdot}4H_2O$) (0.01 mmol)), are dissolved in 10 mL of deionized water. This mixture is slowly added to a 70 mL solution of 10 mol L^{-1} sodium hydroxide (NaOH), with vigorous stirring to produce dark brown precipitates. The mixture is then transferred into a 100 mL polytetrafluoroethylene autoclave and subjected to hydrothermal treatment at 120 °C for 24 h. Subsequently, the precipitates are separated from the solution using centrifugation, followed by extensive washing with deionized water and ethanol to remove impurities. The washed precipitates are then dried under low vacuum conditions at room temperature. The dried brown powders are finely ground using an agate mortar and then annealed in a mixed gas of 5 % H_2 and 95 % Ar at a flow rate of 100 mL min^{-1} at 450 °C for 4 h.

2.2. Characterizations

To identify the crystalline phases of the catalysts, the X-ray Diffraction (XRD) patterns were acquired using a Bruker Advantage D8 diffractometer which employs CuKα radiation and a D/teX Ultra detector. For the surface morphology characterization, the Scanning Electron Microscopy (SEM) images were captured using a Hitachi Regulus SU8100 instrument operated at an accelerating voltage of 5 kV. Additionally, the SEM-energy dispersive X-ray (EDX) mappings were performed using a Bruker XFlash 6–60 detector. The Transmission Electron Microscope (TEM) images, including EDX mapping, were performed using FEI TALOS F200X at an accelerating voltage of 200 kV. Inductively Coupled Plasma Optical Emission Spectroscopy (ICP-OES) measurements were conducted on an Agilent ICP-OES 730 instrument to determine the precise concentration of dopants. The temperature-programmed surface reaction (TPSR) analysis was carried out on a Micromeritics Autochem II 2920 instrument, which is coupled with a Hiden HPR20 mass spectrometer. The detailed experimental procedures of TPSR are described in Note S1 in the Supporting Information. The ultraviolet–visible–near-infrared diffuse reflectance spectroscopy (UV–Vis–NIR DRS) was measured using a Shimadzu UV3600Plus spectrometer in the wavelength range of 300–2500 nm.

2.3. RWGS performance tests

The thermocatalytic RWGS reaction was conducted in a flow reactor (Harrick MRA-5) over a temperature range of 200–600 °C using a reactant gas mixture of 4 % CO_2, 1 % H_2, and 95 % Ar. Prior to testing, the catalysts were pre-activated in the same reaction gas for 20 min at 450 °C. Photothermal RWGS experiments were carried out in a batch reactor (GPRT-100, CEAulight) with the same reactant gas mixture pressurized to 0.3 MPa. A 300 W Xe lamp (wavelength range of 300–2500 nm, CEL-HXF300, CEAuLight) served as the light source. The pre-activation of catalysts was carried out in the same reaction gas under irradiation for 1 h before the reaction. The light intensity was ~1.6 W cm^{-2}, and the surface temperature under illumination was monitored via an integrated thermocouple. Gas products were analyzed using an Agilent 990 micro-gas chromatograph (μGC) equipped with micro-thermal conductivity detectors (μTCD).

3. Results and discussions

To investigate the influence on the thermocatalytic RWGS reaction, first, we incorporated ~0.25 mol% of Co, Ni, and Cu, respectively, into the $Ce_{0.7}Fe_{0.3}O_2$ solid-solution nanorods using a co-precipitation process followed by hydrothermal treatment, as illustrated in Fig. 1a. The catalyst samples were denoted as $M_{0.25\ \%}$:$Ce_{0.7}Fe_{0.3}O_2$ (M = Co, Ni, and Cu). The X-ray diffraction (XRD) patterns revealed clear diffraction peaks at 28.5, 33.1, and 47.5° for all the $M_{0.25\ \%}$:$Ce_{0.7}Fe_{0.3}O_2$ samples, corresponding to the (111), (200), and (220) lattice planes of the fluorite-structured CeO_2 (Fig. 1b). A minor diffraction peak attributed to the (311) plane of Fe_3O_4 was observed at 34.5°, which is reasonable for a 30 mol% Fe doping level and does not affect the successful incorporation of most Fe into the CeO_2 lattices to form a solid-solution structure, consistent with previous literature [24]. No diffraction peaks related to metallic Co, Ni, and Cu, or their oxides were observed. The actual concentrations of transition metals were determined by an inductively coupled plasma emission (ICP) spectrometry (Fig. S1), further confirming the incorporation of metals into the $Ce_{0.7}Fe_{0.3}O_2$ solid-solution nanorods. The SEM images of all the $M_{0.25\ \%}$:$Ce_{0.7}Fe_{0.3}O_2$ samples revealed a nanorod structure with ~100 nm in length (Fig. 1c and Figs. S2–S3). In particular, the EDX mappings of $Co_{0.25\ \%}$:$Ce_{0.7}Fe_{0.3}O_2$, indicating uniform dispersion of Ce, Fe, and additional Co atoms within the nanorod structures without evident metal segregations (Fig. 1c). The high resolution

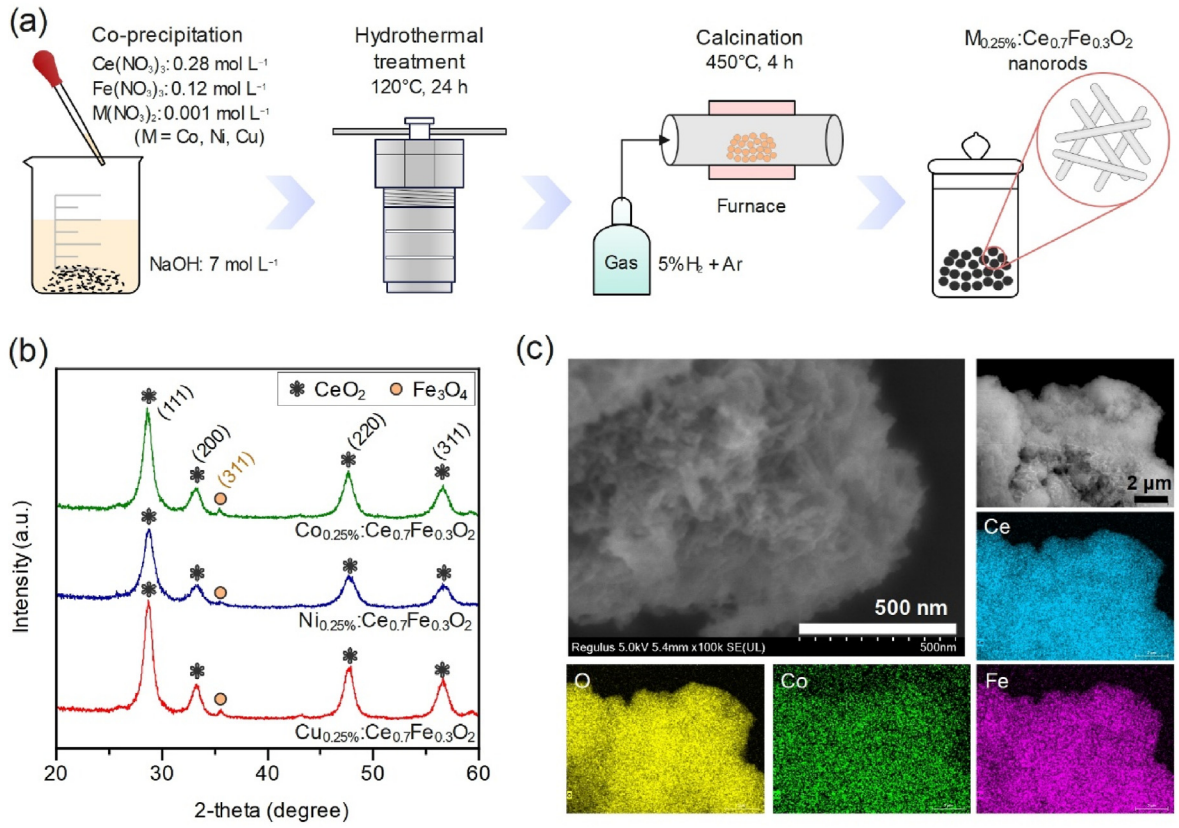

Fig. 1. (a) Schematic illustration of the synthesis process, (b) XRD patterns, and (c) ICP-OES results of $M_{0.25\ \%}$:$Ce_{0.7}Fe_{0.3}O_2$ (M = Co, Ni, and Cu). (d) SEM and (e) EDX mappings of $Co_{0.25\ \%}$:$Ce_{0.7}Fe_{0.3}O_2$.

(HR)-TEM images of $Co_{0.25\ \%}$:$Ce_{0.7}Fe_{0.3}O_2$ (Fig. S4) illustrates lattice fringes with d-spacings of 0.19, 0.27 nm and 0.31 nm, corresponding to the (110), (100) and (111) planes of CeO_2, respectively, aligning with the XRD obesrvasions. The absence of FeO_x and CoO_x particles confirms the uniform dispersion of Fe and Co cations in the CeO_2 lattice, reinforcing the presence of a stable ceria-based solid-solution structure.

We then evaluated the thermocatalytic activities of $M_{0.25\ \%}$:$Ce_{0.7}Fe_{0.3}O_2$ and the pristine $Ce_{0.7}Fe_{0.3}O_2$ catalysts in a flow reactor at a gas-hourly space velocity (GHSV) of 300,000 mL g_{cat}^{-1} h^{-1} with a reactant gas composition of 1 % CO_2, 4 % H_2, and 95 % Ar. As shown in Fig. 2a, all catalysts exhibited RWGS performance, with the catalysts doped with transition metals showing enhanced CO_2 conversion rates compared to the pristine $Ce_{0.7}Fe_{0.3}O_2$ solid solution, with a CO selectivity of ~100 %. Specifically, $Co_{0.25\ \%}$:$Ce_{0.7}Fe_{0.3}O_2$ and $Ni_{0.25\ \%}$:$Ce_{0.7}Fe_{0.3}O_2$ demonstrated the highest improvements, lowering the reaction onset temperature to 250 °C. At 450 °C, the catalytic activity varied notably among the catalysts, with $Co_{0.25\ \%}$:$Ce_{0.7}Fe_{0.3}O_2$ exhibiting the highest activity, achieving a CO conversion rate of 26 % and a ~100 % CO selectivity, outperforming the Ni and Cu-doped catalysts. At 600 °C, the CO_2 conversion of all catalysts showed the same RWGS performance. These results suggest that doping a transitional metal may reduce the activation energy of the RWGS reaction, thereby decreasing the RWGS temperature and enhancing the thermocatalytic activities.

Subsequently, we selected Co as the optimal metal-doping component and then conducted temperature-programmed surface reaction (TPSR) to analyze CO desorption and water generation in the RWGS reaction

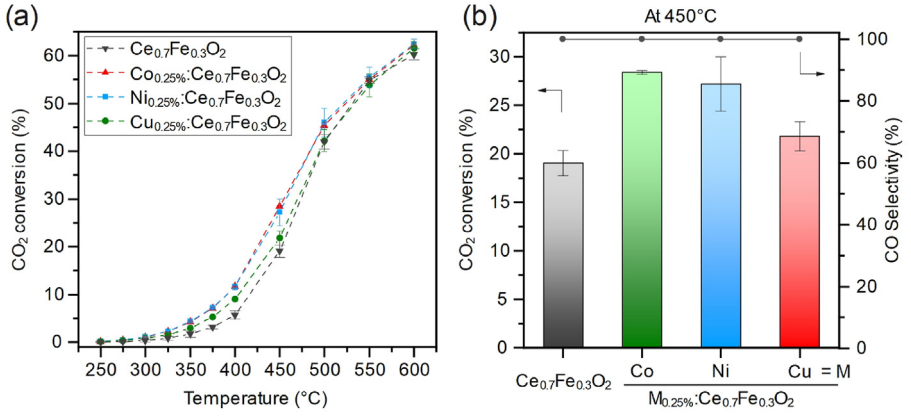

Fig. 2. (a) CO_2 conversion as a function of temperature, and (b) CO production rates at 450 °C in the thermocatalytic RWGS reaction using $M_{0.25\ \%}$:$Ce_{0.7}Fe_{0.3}O_2$ (M = Co, Ni, and Cu).

atmosphere for $Co_{0.25\ \%}$:$Ce_{0.7}Fe_{0.3}O_2$ and $Ce_{0.7}Fe_{0.3}O_2$ catalysts. Typically, there are two mechanisms for the RWGS reaction: the redox mechanism, where the reduction of surface oxygen species is the key step, and the intermediate species decomposition mechanism, where the adsorption of CO_2 and the dissociation of H_2 are the critical steps [25,26]. As depicted in Fig. 3a, after introducing the mixed reaction gas of H_2 and CO_2 for TPSR test, the appearance temperature of H_2O ($m/z = 18$) mass spectrometry (MS) signals was lower than that of the CO signals ($m/z = 28$) for both $Co_{0.25\ \%}$:$Ce_{0.7}Fe_{0.3}O_2$ and $Ce_{0.7}Fe_{0.3}O_2$, indicating the process of surface oxygen reduction to generate H_2O. Therefore, the RWGS reaction on the solid solution catalyst likely follows the redox mechanism, which is consistent with the results in the previous studies on iron-based oxides [27]. A detailed comparison of the two catalysts revealed that Co doping shifted the appearance temperature of H_2O signals in TPSR from ~350 °C to ~320 °C. To further investigate the changes in the surface chemical states of the catalyst during the reaction process, we carried out XPS analysis on the samples before and after the reaction. As shown in Fig. 4, the Fe^{2+}/Fe^{3+} molar ratio in $Co_{0.25\ \%}$:$Ce_{0.7}Fe_{0.3}O_2$ and $Ce_{0.7}Fe_{0.3}O_2$ before the reaction was relatively close, at 0.53 and 0.50, respectively. After the reaction, the Fe^{2+}/Fe^{3+} ratio in the $Co_{0.25\ \%}$:$Ce_{0.7}Fe_{0.3}O_2$ catalyst increased to 1.55, higher than the $Ce_{0.7}Fe_{0.3}O_2$ ratio of 1.28, indicating that Co doping increased H_2 dissociation and facilitated the reduction of Fe^{3+} to Fe^{2+}. In CeO_2-based solid solution structure, the reduction in the oxidation state of cations led to the generation of more oxygen vacancies (V_O). These oxygen vacancies can serve as reaction sites to facilitate CO_2 adsorption and dissociation activation. Therefore, the above results indicate that Co doping enhanced the surface reducibility of the catalyst at lower temperatures, increased the number of surface V_O, and facilitated the formation of active Fe^{2+}–V_O species on the surface, thereby promoting the reduction of CO_2 to CO in the synergistic effect of Co cation doping sites.

The UV–Vis–NIR spectra of all $Co_{x\%}$:$Ce_{0.7}Fe_{0.3}O_2$ samples (Fig. S5) exhibited strong absorption within the 300–2500 nm wavelength range, with absorption rates exceeding 95 % in the UV–Vis region (300–800 nm) and over 85 % in the near-infrared range (800–2500 nm). Therefore, the solid-solution catalysts feature full solar spectrum absorption and have the potential to function as photothermal catalysts by absorbing photons to induce notable thermal effects, raising the surface temperature of the catalyst, and triggering the RWGS reaction [28]. For this reason, we investigate the influence of different Co contents on the performance of the photothermal catalytic RWGS reaction. A photothermal batch reaction was carried out for 1 h using 50 mg $Co_{x\ \%}$:$Ce_{0.7}Fe_{0.3}O_2$ with varying Co doping levels ($x\% = 0.25$ %, 5 %, and 10 %), alongside the mixed reactant gas (1 % CO_2, 4 % H_2, and 95 % Ar) at 0.3 MPa. The reactions were carried out under continuous irradiation from a 300 W Xe lamp light source with a power density of ~1.6 W cm^{-2} and a wavelength range of 300–2500 nm. The surface temperature of the catalyst was measured to be ~450 °C using a thermocouple built into the reactor (Table S1). As shown in Fig. 4a, the CO_2 conversion increased from 28 % to 45 % after the addition of a trace amount of Co (~0.25 mol %) to the non-doped catalyst, while maintaining 100 % CO selectivity, demonstrating the effective promotion of the RWGS reaction even with minimal Co doping. At a Co doping content of 5 mol%, the catalyst exhibited a higher CO_2 conversion rate, 50 %, with a selectivity of 100 %. With an increase in Co content to 10 %, the CO_2 conversion rate increased to 53 % compared to the 5 % Co-content catalyst. However, we observed a shift of the RWGS reaction towards CO_2 methanation and a drop in CO selectivity to ~80 % with $Co_{10\ \%}$:$Ce_{0.7}Fe_{0.3}O_2$. This is attributed to an excess of Co that easily forms strong bonds with dissociated CO, leading to deep hydrogenation to produce methane. Therefore, considering both conversion and selectivity, we consider 5 % Co doping to be optimal. We also confirmed that the photothermal catalytic performance of the reference catalysts, $Co_{x\%}$:CeO_2 (x = 0.25, 5, and 10), without Fe incorporation, was inferior to $Co_{x\%}$:$Ce_{0.7}Fe_{0.3}O_2$ catalysts under the same conditions (Fig. S6). Additionally, XRD results indicated that the solid solution catalyst fabricated through our co-precipitation-hydrothermal synthesis route did not exhibit significant precipitation of Co metal or oxides, even with increased Co doping (Fig. 5c and Fig. S7). Lastly, we assessed the stability of the $Co_{5\%}$:$Ce_{0.7}Fe_{0.3}O_2$ catalyst through 10 sequential 1-h batch photothermal RWGS reactions under a light power density of 1.6 W cm^{-2}. Fig. 5b shows that the conversion of the catalyst remained ~50 % and the selectivity at 100 % throughout the 10 rounds of operations (10 h). We characterized the morphology and structure of the catalyst before and after stability testing. TEM images in Fig. 5a and b revealed that the catalyst maintained a stacked nanorod structure, with EDX elemental mapping confirming the presence of Co, Ce, Fe, and Co uniformly distributed within the solid solution. Compared to the morphology before the reaction, no significant changes were observed post-reaction. The XRD pattern after the reaction remained essentially the same as that before the reaction (Fig. 5c and d), showing only diffraction peaks consistent with the CeO_2 crystal structure and minor Fe_3O_4 precipitates. No precipitation of Co and Co oxides was observed. Only a moderate increase in diffraction peak intensity was observed, which can likely be attributed to crystal growth

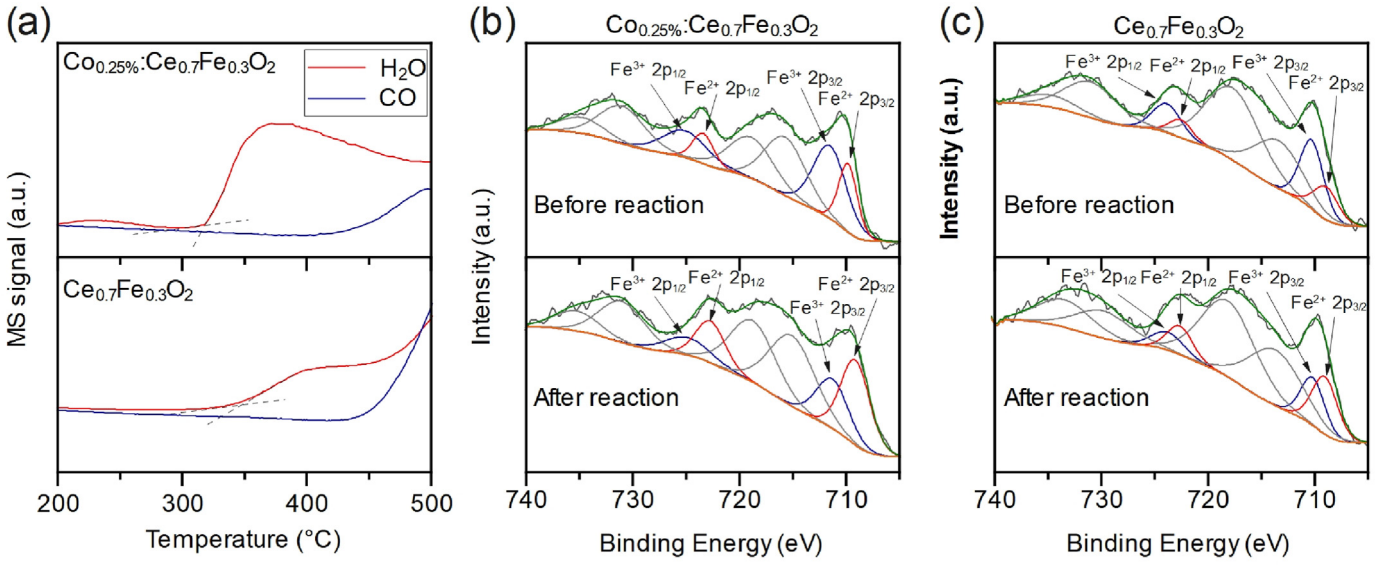

Fig. 3. (a) TPSR results of $Co_{0.25\ \%}$:$Ce_{0.7}Fe_{0.3}O_2$ and $Ce_{0.7}Fe_{0.3}O_2$. XPS spectra of Fe 2p orbitals of (b) $Ce_{0.7}Fe_{0.3}O_2$ and (c) $Co_{0.25\ \%}$:$Ce_{0.7}Fe_{0.3}O_2$.

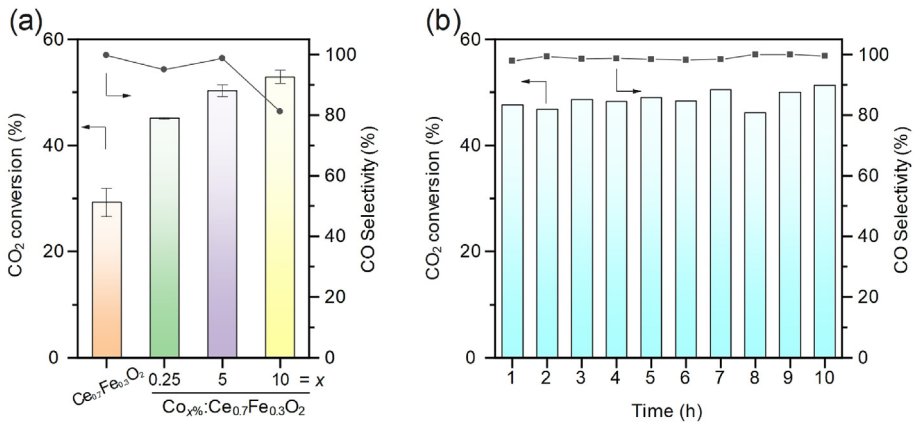

Fig. 4. (a) Photothermal RWGS activities of $Co_{x\%}$:$Ce_{0.7}Fe_{0.3}O_2$ ($_x$ = 0.25, 5, and 10), and (b) catalytic stability of $Co_{x\%}$:$Ce_{0.7}Fe_{0.3}O_2$ in a batch reaction system.

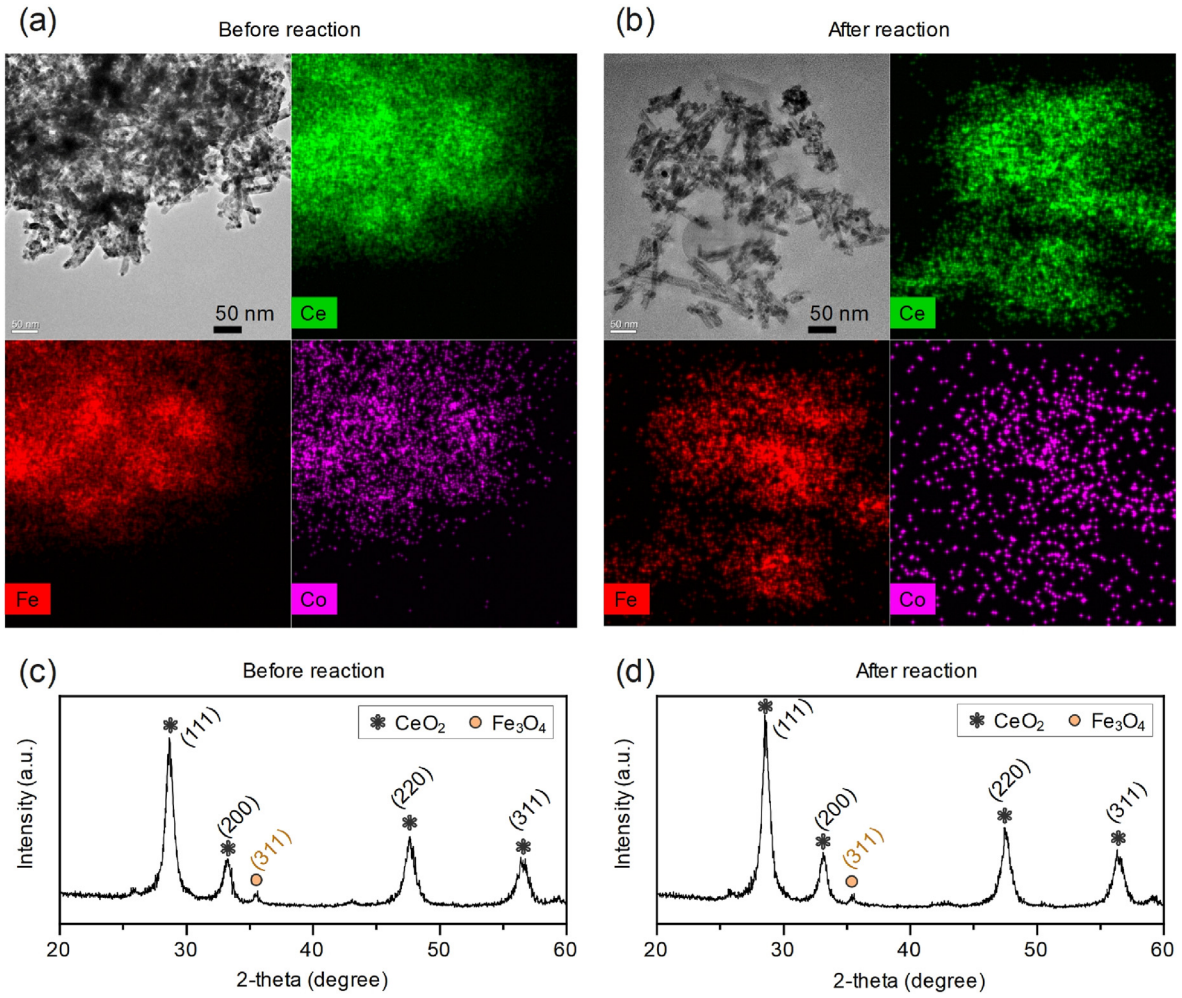

Fig. 5. TEM images and EDX-mappings of $Co_{5\%}$:$Ce_{0.7}Fe_{0.3}O_2$ (a) before and (b) after the stability test. XRD patterns of $Co_{5\%}$:$Ce_{0.7}Fe_{0.3}O_2$ (c) before and (d) after the stability test.

induced by the surface temperature during the photothermal reaction. In summary, $Co_{5\%}$:$Ce_{0.7}Fe_{0.3}O_2$ exhibits good morphology, structure, and RWGS catalytic stability throughout the batch reaction cycles.

4. Conclusions

In summary, this study concentrates on enhancing the activity of Fe oxide-based catalysts for the RWGS reaction by doping them with Co, Ni, and Cu on a solid-solution platform of $Ce_{0.7}Fe_{0.3}O_2$ nanorods. Particularly, 0.25–5 mol% Co-doped $Ce_{0.7}Fe_{0.3}O_2$ can reduce the onset temperature of the RWGS reaction, promote CO_2 conversion at temperatures below 500 °C, and maintain a high selectivity for CO. Detailed analyses including TPSR and XPS analysis revealed enhanced H_2 dissociation and catalyst reducibility with Co doping, facilitating the formation of active

Fe^{2+}–V_O sites for CO_2 adsorption and dissociative activation. Moreover, leveraging the strong light absorption capabilities of Fe-based catalysts, we evaluate the photothermal RWGS performance of the solid-solution catalysts with varying Co doping levels. Remarkably, 5 mol% Co doping displayed optimal activity in batch reactions under 300 W Xe-lamp irradiations, attaining a CO_2 conversion of 50 % within 1 h, a selectivity of ~100 %, and stability over 10 reaction cycles spanning 10 h. This study underscores the potential of synergistic metal dopants in Fe oxide-based catalysts for efficient and selective CO_2 conversion.

Data availability

Data will be made available on request.

CRediT authorship contribution statement

Yi Xie: Investigation. **Wenhao Qin:** Methodology. **Linyu Wang:** Investigation. **Yueren Liu:** Validation. **Haoyang Jiang:** Validation. **Miao Zhong:** Writing – review & editing, Supervision.

Declaration of competing interest

The authors declare that they have no known competing financial interests or personal relationships that could have appeared to influence the work reported in this paper.

Acknowledgments

This work was supported by the National Key R&D Program of China (No. 2020YFA0406102), the National Natural Science Foundation of China (grant number 22272078), the Frontiers Science Center for Critical Earth Material Cycling of Nanjing University, the “Innovation and Entrepreneurship of Talents plan” of Jiangsu Province, and Program for Innovative Talents and Entrepreneurs in Jiangsu (JSSCTD202138) .

Appendix A. Supplementary data

Supplementary data to this article can be found online at https://doi.org/10.1016/j.pnsc.2024.05.011.

References

[1] J. Zhang, C. Guo, S. Fang, X. Zhao, L. Li, H. Jiang, Z. Liu, Z. Fan, W. Xu, J. Xiao, M. Zhong, Accelerating electrochemical CO_2 reduction to multi-carbon products via asymmetric intermediate binding at confined nanointerfaces, Nat. Commun. 14 (2023) 1298, https://doi.org/10.1038/s41467-023-36926-x.

[2] L. Li, Z. Liu, X. Yu, M. Zhong, Achieving high single-pass carbon conversion efficiencies in durable CO_2 electroreduction in strong acids via electrode structure engineering, Angew. Chem. Int. Ed. 62 (2023) e202300226, https://doi.org/10.1002/anie.202300226.

[3] H. Jiang, L. Wang, H. Kaneko, R. Gu, G. Su, L. Li, J. Zhang, H. Song, F. Zhu, A. Yamaguchi, J. Xu, F. Liu, M. Miyauchi, W. Ding, M. Zhong, Light-driven CO_2 methanation over Au-grafted $Ce_{0.95}Ru_{0.05}O_2$ solid-solution catalysts with activities approaching the thermodynamic limit, Nat. Catal. 6 (2023) 519–530, https://doi.org/10.1038/s41929-023-00970-z.

[4] L. Zhou, J.M.P. Martirez, J. Finzel, C. Zhang, D.F. Swearer, S. Tian, H. Robatjazi, M. Lou, L. Dong, L. Henderson, P. Christopher, E.A. Carter, P. Nordlander, N.J. Halas, Light-driven methane dry reforming with single atomic site antenna-reactor plasmonic photocatalysts, Nat. Energy 5 (2020) 61–70, https://doi.org/10.1038/s41560-019-0517-9.

[5] H. Liu, S. Li, W. Wang, W. Yu, W. Zhang, C. Ma, C. Jia, Partially sintered copper–ceria as excellent catalyst for the high-temperature reverse water gas shift reaction, Nat. Commun. 13 (2022) 867, https://doi.org/10.1038/s41467-022-28476-5.

[6] L. Li, A. Ozden, S. Guo, F.P. García De Arquer, C. Wang, M. Zhang, J. Zhang, H. Jiang, W. Wang, H. Dong, D. Sinton, E.H. Sargent, M. Zhong, Stable, active CO_2 reduction to formate via redox-modulated stabilization of active sites, Nat. Commun. 12 (2021) 5223, https://doi.org/10.1038/s41467-021-25573-9.

[7] X. Yu, Y. Xu, L. Li, M. Zhang, W. Qin, F. Che, M. Zhong, Coverage enhancement accelerates acidic CO_2 electrolysis at ampere-level current with high energy and carbon efficiencies, Nat. Commun. 15 (2024) 1711, https://doi.org/10.1038/s41467-024-45988-4.

[8] J. Zhao, X. Guo, R. Shi, G.I.N. Waterhouse, X. Zhang, Q. Dai, T. Zhang, NiFe nanoalloys derived from layered double hydroxides for photothermal synergistic reforming of CH_4 with CO_2, Adv. Funct. Mater. 32 (2022) 2204056, https://doi.org/10.1002/adfm.202204056.

[9] L. Wang, L. Wang, F. Xiao, Tuning product selectivity in CO_2 hydrogenation over metal-based catalysts, Chem. Sci. 12 (2021) 14660–14673, https://doi.org/10.1039/D1SC03109K.

[10] A. Parastaev, V. Muravev, E. Huertas Osta, A.J.F. van Hoof, T.F. Kimpel, N. Kosinov, E.J.M. Hensen, Boosting CO_2 hydrogenation via size-dependent metal–support interactions in cobalt/ceria-based catalysts, Nat. Catal. 3 (2020) 526–533, https://doi.org/10.1038/s41929-020-0459-4.

[11] F. Abild-Pedersen, M.P. Andersson, CO adsorption energies on metals with correction for high coordination adsorption sites – a density functional study, Surf. Sci. 601 (2007) 1747–1753, https://doi.org/10.1016/j.susc.2007.01.052.

[12] Z. Li, J. Liu, R. Shi, G.I.N. Waterhouse, X. Wen, T. Zhang, Fe-Based catalysts for the direct photohydrogenation of CO_2 to value-added hydrocarbons, Adv. Energy Mater. 11 (2021) 2002783, https://doi.org/10.1002/aenm.202002783.

[13] C. Vogt, E. Groeneveld, G. Kamsma, M. Nachtegaal, L. Lu, C.J. Kiely, P.H. Berben, F. Meirer, B.M. Weckhuysen, Unravelling structure sensitivity in CO_2 hydrogenation over nickel, Nat. Catal. 1 (2018) 127–134, https://doi.org/10.1038/s41929-017-0016-y.

[14] H. Yue, Y. Zhao, S. Zhao, B. Wang, X. Ma, J. Gong, A copper-phyllosilicate core-sheath nanoreactor for carbon–oxygen hydrogenolysis reactions, Nat. Commun. 4 (2013) 2339, https://doi.org/10.1038/ncomms3339.

[15] D.H. Kim, S.W. Han, H.S. Yoon, Y.D. Kim, Reverse water gas shift reaction catalyzed by Fe nanoparticles with high catalytic activity and stability, J. Ind. Eng. Chem. 23 (2015) 67–71, https://doi.org/10.1016/j.jiec.2014.07.043.

[16] C. Song, X. Liu, M. Xu, D. Masi, Y. Wang, Y. Deng, M. Zhang, X. Qin, K. Feng, J. Yan, J. Leng, Z. Wang, Y. Xu, B. Yan, S. Jin, D. Xu, Z. Yin, D. Xiao, D. Ma, Photothermal conversion of CO_2 with tunable selectivity using Fe-based catalysts: from oxide to carbide, ACS Catal. 10 (2020) 10364–10374, https://doi.org/10.1021/acscatal.0c02244.

[17] Y. Meng, X. Liu, M. Bai, J. Chen, Y. Ma, X. Wen, Adsorption or deoxidation of H_2 interacted with Fe_3O_4 surface under different H coverage: a DFT study, Appl. Surf. Sci. 502 (2020) 144097, https://doi.org/10.1016/j.apsusc.2019.144097.

[18] H. Shen, Y. Dong, S. Yang, Y. He, Q. Wang, Y. Cao, W. Wang, T. Wang, Q. Zhang, H. Zhang, Identifying the roles of Ce^{3+}−OH and Ce−H in the reverse water-gas shift reaction over highly active Ni-doped CeO_2 catalyst, Nano Res. 15 (2022) 5831–5841, https://doi.org/10.1007/s12274-022-4207-8.

[19] C. Alvarez-Galvan, P.G. Lustemberg, F.E. Oropeza, B. Bachiller-Baeza, M. Dapena Ospina, M. Herranz, J. Cebollada, L. Collado, J.M. Campos-Martin, V.A. De La Peña-O'Shea, J.A. Alonso, M.V. Ganduglia-Pirovano, Highly active and stable Ni/La-doped ceria material for catalytic CO_2 reduction by reverse water-gas shift reaction, ACS Appl. Mater. Interfaces 14 (2022) 50739–50750, https://doi.org/10.1021/acsami.2c11248.

[20] F. Jiang, S. Wang, B. Liu, J. Liu, L. Wang, Y. Xiao, Y. Xu, X. Liu, Insights into the influence of CeO_2 crystal facet on CO_2 hydrogenation to methanol over Pd/CeO_2 catalysts, ACS Catal. 10 (2020) 11493–11509, https://doi.org/10.1021/acscatal.0c03324.

[21] Y. Tang, Y. Wei, Z. Wang, S. Zhang, Y. Li, L. Nguyen, Y. Li, Y. Zhou, W. Shen, F.F. Tao, P. Hu, Synergy of single-atom Ni1 and Ru1 sites on CeO2 for dry reforming of CH4, J. Am. Chem. Soc. 141 (2019) 7283–7293, https://doi.org/10.1021/jacs.8b10910.

[22] M. Gu, S. Dai, R. Qiu, M.E. Ford, C. Cao, I.E. Wachs, M. Zhu, Structure–activity relationships of copper- and potassium-modified iron oxide catalysts during reverse water–gas shift reaction, ACS Catal. 11 (2021) 12609–12619, https://doi.org/10.1021/acscatal.1c03792.

[23] S. Ning, H. Xu, Y. Qi, L. Song, Q. Zhang, S. Ouyang, J. Ye, Microstructure induced thermodynamic and kinetic modulation to enhance CO_2 photothermal reduction: a case of atomic-scale dispersed Co–N species anchored Co@C hybrid, ACS Catal. (2020), https://doi.org/10.1021/acscatal.9b04963.

[24] T.R. Sahoo, M. Armandi, R. Arletti, M. Piumetti, S. Bensaid, M. Manzoli, S.R. Panda, B. Bonelli, Pure and Fe-doped CeO_2 nanoparticles obtained by microwave assisted combustion synthesis: physico-chemical properties ruling their catalytic activity towards CO oxidation and soot combustion, Appl. Catal. B Environ. 211 (2017) 31–45, https://doi.org/10.1016/j.apcatb.2017.04.032.

[25] L.F. Bobadilla, J.L. Santos, S. Ivanova, J.A. Odriozola, A. Urakawa, Unravelling the role of oxygen vacancies in the mechanism of the reverse water–gas shift reaction by operando DRIFTS and ultraviolet–visible spectroscopy, ACS Catal. 8 (2018) 7455–7467, https://doi.org/10.1021/acscatal.8b02121.

[26] M. Zhu, Q. Ge, X. Zhu, Catalytic reduction of CO_2 to CO via reverse water gas shift reaction: recent advances in the design of active and selective supported metal catalysts, Trans. Tianjin Univ. 26 (2020) 172–187, https://doi.org/10.1007/s12209-020-00246-8.

[27] M. Zhu, I.E. Wachs, Resolving the reaction mechanism for H_2 formation from high-temperature water–gas shift by chromium–iron oxide catalysts, ACS Catal. 6 (2016) 2827–2830, https://doi.org/10.1021/acscatal.6b00659.

[28] G. Wang, X. Mu, J. Li, Q. Zhan, Y. Qian, X. Mu, L. Li, Light-induced nonoxidative coupling of methane using stable solid solutions, Angew. Chem. Int. Ed. 60 (2021) 20760–20764, https://doi.org/10.1002/anie.202108870.